Environmental Fluid Mechanics (2019) 19:111–135
https://doi.org/10.1007/s10652-018-9621-9

ORIGINAL ARTICLE

An analytical model of an urban heat island circulation in calm conditions

Alan Shapiro[1,2] · **Evgeni Fedorovich**[1]

Received: 11 April 2018 / Accepted: 13 August 2018 / Published online: 21 August 2018

Abstract
We obtain an analytical model solution to an idealization of an urban heat island (UHI) circulation—the steady shallow convective flow of a viscous stably stratified fluid over a differentially heated lower boundary without system rotation (no Coriolis force) or background wind. The coupled linearized equations of motion and thermal energy are solved for flows in two-dimensional Cartesian (slab-symmetric) and axisymmetric geometries forced by laterally varying surface buoyancies considered as Gaussian and parabolic arch functions. The scaled problem is free of governing parameters, and the solutions are universal. In all cases the flow is dominated by an in-up-out circulation. The updraft is stronger in the axisymmetric case than in the slab-symmetric case, while the surrounding downdraft, and the inflow and outflow branches of the circulation are stronger in the slab-symmetric case. These differences are explained in terms of the response of the perturbation pressure to the thermal forcing in the different geometries. The scalings themselves provide insight into observations that daytime UHI circulations can be stronger than nighttime circulations despite the relative weakness of urban–rural temperature contrasts during the daytime.

Keywords Buoyantly driven circulation · Stratified fluid · Turbulent Prandtl number · Urban heat island

1 Introduction

The urban heat island (UHI) refers to the state of warmth of a large urban complex relative to its rural surroundings [60]. Although urban areas are often warmer than their surroundings during the afternoon and nighttime hours, the urban–rural temperature contrasts are usually the strongest at night, particularly when skies are clear and background winds are weak. These contrasts are typically 1–2 K during the day [16, 34, 36, 42] and 5–8 K at night [58, 59], though with much spatial and temporal variability associated with size of the urban complex, land use, vegetation, topography, meteorological conditions, and

✉ Alan Shapiro
ashapiro@ou.edu

[1] School of Meteorology, University of Oklahoma, 120 David L. Boren Blvd., Norman, OK, USA

[2] Center for Analysis and Prediction of Storms, University of Oklahoma, 120 David L. Boren Blvd., Norman, OK, USA

season [12, 38, 42, 78, 85]. The relatively warm air in the UHI (sometimes referred to as a heat dome) is often capped by a crossover layer in which the air is cooler than in the rural environment at the same elevation, though the horizontal temperature gradient in that layer is not as strong as in the heat dome [6, 17, 59, 60, 74, 77]. The thermodynamic and dynamical characteristics of UHIs are reviewed in Garstang et al. [30], Oke [59, 60], Bornstein [8], Fernando et al. [26], Arnfield [2], and Kanda [41]. The environmental, social, and economic impacts of UHIs are reviewed in Phelan et al. [62].

A dynamical feature of particular importance for urban air quality and weather is the mesoscale circulation generated by urban–rural temperature contrasts in UHIs [5, 7, 9, 19, 23, 24, 27, 29, 34, 36, 49, 52, 63, 69, 70, 81]. In its most idealized form (associated with low background wind speeds), the urban heat island circulation[1] (UHIC) consists of an updraft extending over much of the urban area, a compensating downdraft over the rural surroundings, low-level convergent inflow, and divergent flow aloft. The UHIC can extend horizontally two or three times the diameter of a city [25, 34, 49]. Remarkably, despite the nighttime maximum in urban–rural temperature contrasts, the UHIC in conditions of weak background winds can be strongest during the daytime [7, 29, 49, 69, 70, 81], although nocturnal preferences for the stronger UHIC have also been documented [5, 19].

UHICs can be difficult to detect in observational datasets. Due to inhomogeneities in the urban setting associated with city morphology, orography, and the presence of parks and urban forests, the signatures of a UHIC may be conflated with the signatures of small-scale intra-urban circulations [20, 50, 75]. Additionally, in locations where an urban area is close to mountains or large bodies of water, a UHIC may interact with a slope flow, sea breeze, or other mesoscale circulation [26–29, 31, 39, 63, 84]. Moreover, even in relatively benign synoptic conditions, background winds can be as strong as UHIC winds. Because of these complexities, UHICs are often studied as idealized flows in controlled experiments using analytical [3, 4, 33, 43, 44, 54, 61, 71, 80], numerical [15, 21, 33, 35, 36, 43, 45, 49, 55, 56, 66], or laboratory [11, 22, 43, 45, 51, 52, 57, 64] models.

In this paper we revisit an analytical description of one of the basic conceptual models of a UHIC—the steady shallow convective flow of a viscous and diffusive stably stratified fluid over a differentially heated lower boundary without system rotation (no Coriolis force) or background wind. Our work puts on record solutions for such flows driven by the same specified surface buoyancy function but considered in slab-symmetric and axisymmetric geometries. Our approach is similar to the linear analyses conducted in Kimura [43] (hereafter K75), and we offer a disclaimer similar to the one therein: we seek insights into the basic dynamical response of the atmosphere to the differential heating of the underlying surface, but do not directly simulate a heat island circulation.

Our study has several features in common with previous linear analyses of heat island circulations and related phenomena, which we now review. Attention is restricted to analyses in which a thermal energy equation (containing a thermal diffusion term that mediates the heating of the atmosphere by the underlying surface) is used along with the equations of motion to couple the dynamical and thermal fields. In his classification of wind types, Jeffreys [40] described antitripic[2] winds, a class of atmospheric motions that includes

[1] Also known as an urban breeze (e.g., [49]), urban breeze circulation (UBC; e.g., [66]), country breeze (e.g., [5]), country wind (e.g., [27]), or buoyancy and turbulence driven atmospheric circulation (BTDAC; e.g., [24]).

[2] Defined as flows in which the frictional terms in the equations of motion are larger than the Coriolis and acceleration terms.

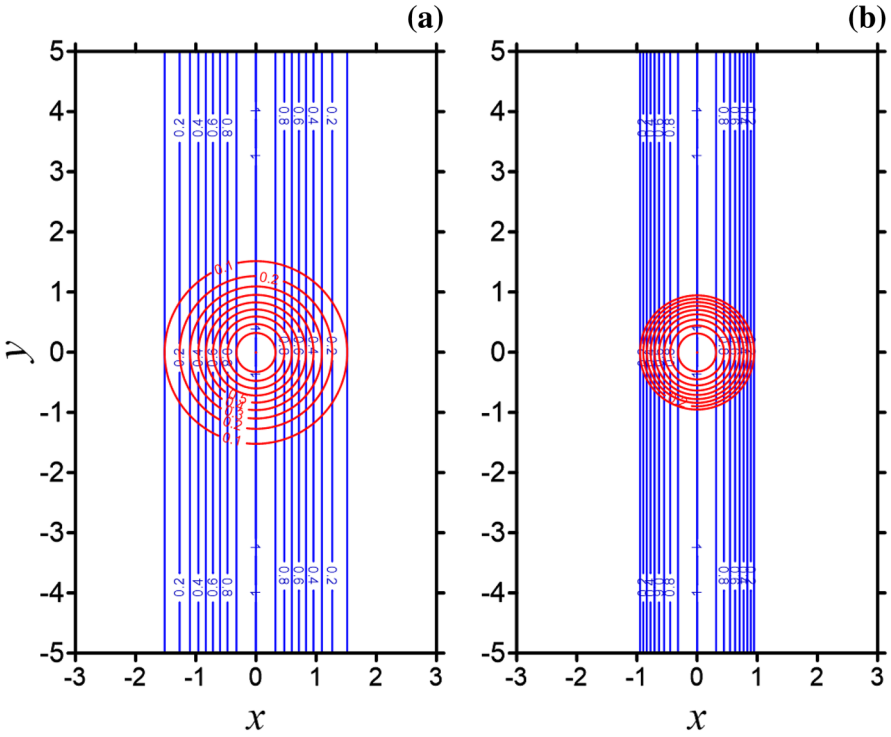

Fig. 1 Horizontal (x–y) plots of non-dimensional surface buoyancy functions f in the forms of **a** Gaussian and **b** parabolic arch functions. Blue lines depict slab-symmetric functions. Red lines depict axisymmetric functions

land and sea breezes. The linearized two-dimensional Cartesian (slab-symmetric) equations of motion and thermal energy were solved for the steady motion of a viscous stably stratified fluid over a lower boundary whose temperature varied laterally as a sinusoid. No provision was made for the Coriolis force, a background wind, or height variations in the eddy viscosity or diffusivity coefficients. A quasi-linearized skin friction condition was imposed on the horizontal wind field at the ground. Based on the structure of the derived wind profile, including the existence of a return flow aloft, Jeffreys [40] concluded that his theory provided a good first approximation to the sea breeze. In a study of factors controlling the depth of oceanic currents, Stommel and Veronis [73] presented solutions for a slab-symmetric scenario similar to that of Jeffrey's [40] sea breeze example, both with and without the Coriolis force (with additional approximations made in the former case), and with the no-slip condition used in place of the skin friction condition. A zone of what would now be referred to as a crossover layer appears in their Fig. 1. K75 extended the Stommel and Veronis [73] framework (version without Coriolis force) to cases where the surface temperature varied laterally as a rectangle (top hat) function, representing a heat island, and a series of rectangle functions, representing a row of heat islands. Although mostly concerned with the slab-symmetric configuration, K75 briefly presented results for axisymmetric forcing, with a focus on the temperature field. However, the axisymmetric temperature solution did not reduce to the same (rectangle) function at the ground as in the

slab-symmetric case, and actually became singular immediately beyond the outer edge of the heat island (K75, footnote on p. 443). In a follow-up study, Kimura [44] extended his slab-symmetric heat island analysis to include a constant background wind U. That study included a more thorough exploration of a solution originally given in Olfe and Lee [61] on viscous effects in urban heat island flows, although the latter also made provision for smoothly varying surface temperature distributions, such as a Gaussian function. Olfe and Lee [61] also analyzed flows forced by an axisymmetric surface heating, but the viscous term in that application was neglected, so their solutions were restricted to infinite Prandtl number.

The layout of our paper is as follows. In Sect. 2 we present the governing equations for a shallow axisymmetric convective flow over a differentially heated surface for a general class of surface buoyancy functions, deduce the scalings for the flow variables, and provide a solution framework using Hankel transforms. The corresponding slab-symmetric problem and its solution in terms of Fourier transforms are described in Sect. 3. In Sect. 4 we consider axisymmetric and slab-symmetric flows driven by surface buoyancy functions in the form of Gaussian and parabolic arch functions. In Sect. 5 we discuss how the geometry of the forcing impacts circulation strength, and describe the implications of the scalings for the timing (day vs. night) of peak circulation strength. A summary follows in Sect. 6.

2 Governing equations and solution framework for axisymmetric shallow convection flow

Consider the steady flow of a stably stratified fluid induced by an axisymmetrically heated lower surface. There is no ambient wind, and the Coriolis force is neglected. We work with the linearized Boussinesq governing equations with the turbulent heat and momentum fluxes parameterized using K-theory (eddy viscosity approach). The kinematic eddy viscosity ν and thermal eddy diffusivity κ are considered constant, but may differ from one another. We write the Reynolds-averaged (mean) governing equations in cylindrical coordinates as

$$0 = -\frac{\partial \Pi}{\partial R} + \nu \frac{\partial^2 U}{\partial Z^2}, \tag{2.1}$$

$$0 = -\frac{\partial \Pi}{\partial Z} + B, \tag{2.2}$$

$$0 = -WN^2 + \kappa \frac{\partial^2 B}{\partial Z^2}, \tag{2.3}$$

$$\frac{1}{R}\frac{\partial (RU)}{\partial R} + \frac{\partial W}{\partial Z} = 0. \tag{2.4}$$

Equation (2.1) is the radial equation of motion, (2.2) is the hydrostatic equation, (2.3) is the thermal energy equation, and (2.4) is the incompressibility condition. Here R is the radial coordinate, Z is the vertical coordinate ($Z=0$ corresponds to the ground), U and W are the radial and vertical mean velocity components, respectively, $B \equiv g\,[\theta - \theta_e(Z)]/\theta_0$ is mean buoyancy [g is acceleration due to gravity, θ is mean potential temperature, θ_e is a base-state potential temperature profile, considered to vary linearly with Z, θ_0 is a constant

reference value of potential temperature], and $\Pi \equiv [p - p_e(Z)]/\rho_0$ is the mean kinematic pressure perturbation [p is mean pressure, p_e is the base-state pressure profile, ρ_0 is a constant reference value of density]. The Brunt-Väisälä frequency $N \equiv \sqrt{(g/\theta_0)\, d\theta_e/dZ}$ is also constant (consistent with linear-in-Z variation of θ_e). Equations (2.1) and (2.3) have undergone a boundary-layer approximation in which the horizontal stress and diffusion terms were neglected. The approximation is based on the presumed smallness of the vertical length scale relative to the lateral length scale, and is justified below.

Taking the vertical derivative of (2.1) and (2.3), and using (2.2) and (2.4) to eliminate Π and W from the resulting equations yield the y-component vorticity equation,

$$0 = -\frac{\partial B}{\partial R} + \nu \frac{\partial^3 U}{\partial Z^3}, \tag{2.5}$$

($\partial U/\partial Z$ is boundary-layer approximated vorticity; $-\partial B/\partial R$ is baroclinic term) and

$$0 = \frac{N^2}{R}\frac{\partial (RU)}{\partial R} + \kappa \frac{\partial^3 B}{\partial Z^3}. \tag{2.6}$$

Attention is restricted to surface buoyancies in the form:

$$B(R,\ 0) = B_0 f(R), \tag{2.7}$$

where B_0 is the peak surface buoyancy and $f(R)$ is a non-dimensional shape function. The latter has a peak magnitude of unity at the city center ($R=0$), is characterized by a single length scale D that quantifies the radial decay rate, and vanishes as $R \to \infty$. We will refer to $R=D$ as the city limit.

A vertical length scale H and radial velocity scale U_0 can be inferred from scale analyses of (2.5) and (2.6) ($B_0/D \sim \nu U_0/H^3$ and $N^2 U_0/D \sim \kappa B_0/H^3$) as

$$U_0 = \frac{B_0}{N\,\mathrm{Pr}^{1/2}}, \quad H = \frac{\nu^{1/3} D^{1/3}}{N^{1/3}\,\mathrm{Pr}^{1/6}}, \tag{2.8}$$

where $\mathrm{Pr} \equiv \nu/\kappa$ is the turbulent Prandtl number. Incorporating (2.8) into a scale analysis of (2.3) or (2.4) yields the vertical velocity scale W_0 as

$$W_0 = \frac{B_0\, \nu^{1/3}}{N^{4/3} D^{2/3}\, \mathrm{Pr}^{2/3}}. \tag{2.9}$$

Apart from notational differences, these length and velocity scales are the same as in the Niino et al. [56] analysis of slab-symmetric flows with a step change in buoyancy.

The ratios of the (omitted) horizontal stress and diffusion terms to vertical stress and diffusion terms scale as $\alpha^2 \equiv (H/D)^2 = \nu^{2/3}/(D^{4/3} N^{2/3}\, \mathrm{Pr}^{1/3})$. Upper bounds on α^2 for city sizes in a $D=1$–50 km range, eddy viscosities in a $\nu = 0.1 - 50\,\mathrm{m^2\,s^{-1}}$ range, Prandtl numbers in a $\mathrm{Pr}=0.3$–10 range, and a Brunt–Väisälä frequency of $N = 0.01\ \mathrm{s^{-1}}$, vary from $\alpha^2 \sim 1 \times 10^{-6}$ to $\alpha^2 \sim 4 \times 10^{-2}$. Since these values are much less than 1, we are justified in neglecting the horizontal stress and diffusion terms in our analysis. Similarly, Niino et al. [56] found that for typical atmospheric conditions and $\mathrm{Pr}=1$, their numerically simulated flows (with horizontal stress and diffusion terms retained) were insensitive to the assigned value of α.

In terms of the non-dimensional variables

$$u(r,z) \equiv \frac{U}{U_0}, \quad w(r,z) \equiv \frac{W}{W_0}, \quad b(r,z) \equiv \frac{B}{B_0}, \quad r \equiv \frac{R}{D}, \quad z \equiv \frac{Z}{H}, \tag{2.10}$$

equations (2.5) and (2.6) become

$$0 = -\frac{\partial b}{\partial r} + \frac{\partial^3 u}{\partial z^3}, \tag{2.11}$$

$$0 = \frac{1}{r}\frac{\partial (ru)}{\partial r} + \frac{\partial^3 b}{\partial z^3}. \tag{2.12}$$

Taking $\partial/\partial r$ of (2.12) and using (2.11) to eliminate $\partial b/\partial r$ from the resulting equation yields

$$\frac{\partial^6 u}{\partial z^6} + \frac{\partial}{\partial r}\left[\frac{1}{r}\frac{\partial (ru)}{\partial r}\right] = 0. \tag{2.13}$$

We solve (2.13) for u using the method of Hankel transforms (e.g., Debnath and Bhatta [14]; hereafter DB) and standard results for Bessel functions (e.g., Abramowitz and Stegun [1]; hereafter AS). Readers not interested in the solution details for this or the slab-symmetric case (Sect. 3) can safely skip to Sect. 4.

The nth order Hankel transform of a function $q(r, z)$ is defined by

$$\hat{q}^n(k, z) \equiv \int_0^\infty q(r, z) r J_n(kr) dr, \tag{2.14}$$

where $J_n(kr)$ is a Bessel function of the first kind of order n and k is a constant. The function q is related to its transform $\hat{q}^n$ through the inversion formula

$$q(r, z) = \int_0^\infty \hat{q}^n(k, z) k J_n(kr) dk. \tag{2.15}$$

Multiplying (2.13) by $rJ_1(kr)$, and integrating the resulting equation with respect to r from $r=0$ to $r=\infty$ produces

$$\frac{d^6 \hat{u}^1}{dz^6} + \left[J_1(kr)\frac{\partial (ru)}{\partial r} - kruJ_0(\xi)\right]\Bigg|_0^\infty + k^2 \int_0^\infty ru\frac{d}{d\xi} J_0(\xi)\, dr = 0, \tag{2.16}$$

where $\xi \equiv kr$, and we have used $d/d\xi\,[\xi J_1(\xi)] = \xi J_0(\xi)$ [(9.1.30) of AS]. Since (i) $J_1(kr)$ and u vanish as $r \to 0$ and $J_0(0) = 1$, (ii) u, $J_0(kr)$, and $J_1(kr)$ vanish as $r \to \infty$ [we assume $\partial u/\partial r J_1(kr)$ and $uJ_0(kr)$ vanish faster than $1/r$ as $r \to \infty$], and (iii) $d/d\xi\, J_0(\xi) = -J_1(\xi)$ [(9.1.28) of AS], (2.16) reduces to

$$\frac{d^6 \hat{u}^1}{dz^6} - k^2 \hat{u}^1 = 0. \tag{2.17}$$

The general solution of (2.17) is

$$\hat{u}^1 = \sum_{i=1}^{6} a_i e^{m_i z}, \tag{2.18}$$

where the constant coefficients a_i will be determined by the boundary conditions, and the m_i are the roots of $m^6 - k^2 = 0$:

$$\begin{aligned} &m_1 = k^{1/3}, \quad m_2 = e^{\pi i/3}k^{1/3}, \quad m_3 = e^{-\pi i/3}k^{1/3} = m_2^*, \quad m_4 = -k^{1/3} = -m_1, \\ &m_5 = -e^{\pi i/3}k^{1/3} = -m_2, \quad m_6 = -e^{-\pi i/3}k^{1/3} = -m_3 = -m_2^* = m_5^*, \end{aligned} \tag{2.19}$$

an asterisk denoting complex conjugation. To prevent an unphysical blow-up of the solution as $z \to \infty$, we reject the roots with positive real parts, taking

$$a_1 = 0, \quad a_2 = 0, \quad a_3 = 0. \tag{2.20}$$

Applying the impermeability condition $W(R,\ 0) = 0$ in (2.3) yields $d^2B\,/\,dZ^2 = 0$ at $Z{=}0$. Evaluating $d^2\,/\,dZ^2$ of (2.5) at $Z{=}0$ then yields $d^5U\,/\,dZ^5 = 0$ at $Z{=}0$. Applying (2.18) in this latter equation (non-dimensionalized) and using (2.19) and (2.20) yields

$$a_4 + e^{-\pi i/3}a_5 + e^{\pi i/3}a_6 = 0. \tag{2.21}$$

To relate the coefficients to the surface buoyancy, multiply (2.11) by $rJ_1(kr)$, and integrate the resulting equation with respect to r, using $d\,/\,d\xi\,[\xi J_1(\xi)] = \xi J_0(\xi)$. We obtain (for all z):

$$\frac{d^3\hat{u}^1}{dz^3} + k\hat{b}^0 = 0. \tag{2.22}$$

Evaluating (2.22) at $z{=}0$ using non-dimensionalized (2.7) gives $d^3\hat{u}^1\,/\,dz^3 = -k\hat{f}^0$ at $z{=}0$. Applying (2.18) in this result then yields:

$$a_4 - a_5 - a_6 = \hat{f}^0. \tag{2.23}$$

Applying the no-slip condition [$U(R,\,0){=}0$, so $\hat{u}^1(k,0) = 0$] in (2.18) provides

$$a_4 + a_5 + a_6 = 0. \tag{2.24}$$

Equations (2.20), (2.21), and (2.24) yield a_4, a_5, and a_6 as

$$a_4 = \frac{1}{2}\hat{f}^0, \quad a_5 = -\frac{1}{4\sqrt{3}}\hat{f}^0(\sqrt{3}+i), \quad a_6 = -\frac{1}{4\sqrt{3}}\hat{f}^0(\sqrt{3}-i) = a_5^*, \tag{2.25}$$

where we have used $e^{\pm\pi i/3} = \cos(\pi\,/\,3) \pm i\,\sin(\pi\,/\,3) = (1 \pm i\sqrt{3})\,/\,2$. Since $a_6 = a_5^*$ and $m_6 = m_5^*$, we see that $a_5\,e^{m_5 z} + a_6\,e^{m_6 z} = a_5\,e^{m_5 z} + (a_5\,e^{m_5 z})^* = 2\mathrm{Re}(a_5\,e^{m_5 z})$, and (2.18) gives

$$\hat{u}^1 = \frac{1}{2}\hat{f}^0\exp\left(-k^{1/3}z\right) - \frac{1}{2\sqrt{3}}\hat{f}^0\mathrm{Re}\left[(\sqrt{3}+i)\exp\left(-e^{\pi i/3}k^{1/3}z\right)\right], \tag{2.26}$$

which simplifies to

$$\hat{u}^1 = \hat{f}^0\left[\frac{1}{2}\mathrm{e}^{-k^{1/3}z} - \frac{1}{\sqrt{3}}\mathrm{e}^{-k^{1/3}z/2}\cos\left(\frac{\sqrt{3}}{2}k^{1/3}z - \frac{\pi}{6}\right)\right]. \tag{2.27}$$

Applying this result in (2.22) yields $\hat{b}^0$ as

$$\hat{b}^0 = \hat{f}^0\left[\frac{1}{2}\mathrm{e}^{-k^{1/3}z} + \frac{1}{\sqrt{3}}\mathrm{e}^{-k^{1/3}z/2}\cos\left(\frac{\sqrt{3}}{2}k^{1/3}z - \frac{\pi}{6}\right)\right]. \tag{2.28}$$

Applying $\hat{b}^0$ in $\hat{w}^0 = d^2\hat{b}^0/dz^2$ [transform of non-dimensionalized (2.3)] yields $\hat{w}^0$ as

$$\hat{w}^0 = \hat{f}^0 k^{2/3}\left[\frac{1}{2}\mathrm{e}^{-k^{1/3}z} - \frac{1}{\sqrt{3}}\mathrm{e}^{-k^{1/3}z/2}\cos\left(\frac{\sqrt{3}}{2}k^{1/3}z + \frac{\pi}{6}\right)\right]. \tag{2.29}$$

Application of (2.15) to the transformed variables provides the solution:

$$u = \int_0^\infty kJ_1(kr)\hat{f}^0\left[\frac{1}{2}\mathrm{e}^{-k^{1/3}z} - \frac{1}{\sqrt{3}}\mathrm{e}^{-k^{1/3}z/2}\cos\left(\frac{\sqrt{3}}{2}k^{1/3}z - \frac{\pi}{6}\right)\right]dk, \tag{2.30}$$

$$b = \int_0^\infty kJ_0(kr)\hat{f}^0\left[\frac{1}{2}\mathrm{e}^{-k^{1/3}z} + \frac{1}{\sqrt{3}}\mathrm{e}^{-k^{1/3}z/2}\cos\left(\frac{\sqrt{3}}{2}k^{1/3}z - \frac{\pi}{6}\right)\right]dk, \tag{2.31}$$

$$w = \int_0^\infty k^{5/3}J_0(kr)\hat{f}^0\left[\frac{1}{2}\mathrm{e}^{-k^{1/3}z} - \frac{1}{\sqrt{3}}\mathrm{e}^{-k^{1/3}z/2}\cos\left(\frac{\sqrt{3}}{2}k^{1/3}z + \frac{\pi}{6}\right)\right]dk. \tag{2.32}$$

Integrating the non-dimensional form of (2.2) with respect to z yields the non-dimensional kinematic pressure perturbation $p \equiv \Pi/(B_0H)$ as $p = -\int_z^\infty b(r,z')dz'$, or, after use of (2.31):

$$p = -\int_0^\infty k^{2/3}J_0(kr)\hat{f}^0\left[\frac{1}{2}\mathrm{e}^{-k^{1/3}z} + \frac{1}{\sqrt{3}}\mathrm{e}^{-k^{1/3}z/2}\cos\left(\frac{\sqrt{3}}{2}k^{1/3}z + \frac{\pi}{6}\right)\right]dk. \tag{2.33}$$

To help visualize the flow, we will plot the Stokes stream function ψ, a function whose isolines are streamlines (e.g., Kundu and Cohen [47]). This function satisfies $u = r^{-1}\partial\psi/\partial z$ and $w = -r^{-1}\partial\psi/\partial r$. Multiplying the latter equation by $rJ_0(kr)$ and integrating the result gives

$$\int_0^\infty rJ_0(kr)w\,dr = -\left[\psi J_0(kr)\right]\Big|_0^\infty - k\int_0^\infty J_1(kr)\psi\,dr. \tag{2.34}$$

Since the ground is impermeable and there are no mass sources along the central axis, ψ has the same constant value along the ground and central axis. Without loss of generality, we set this constant to zero, and write (2.34) as

$$\int_0^\infty rJ_0(kr)w\,dr = -k\int_0^\infty rJ_1(kr)\,\phi\,dr, \tag{2.35}$$

where $\phi \equiv \psi/r$ is a modified Stokes stream function. Equation (2.35) can be recognized as

$$\hat{w}^0 = -k\hat{\phi}^1. \tag{2.36}$$

With $\hat{w}^0$ obtained from (2.29), we get $\hat{\phi}^1$ from (2.36), ϕ from the inverse transform (2.15) of $\hat{\phi}^1$, and then $\psi = r\phi$ from

$$\psi = -r\int_0^\infty k^{2/3}J_1(kr)\hat{f}^0\left[\frac{1}{2}e^{-k^{1/3}z} - \frac{1}{\sqrt{3}}e^{-k^{1/3}z/2}\cos\left(\frac{\sqrt{3}}{2}k^{1/3}z + \frac{\pi}{6}\right)\right]dk. \quad (2.37)$$

3 Slab-symmetric shallow convection flow

We now consider the circulation induced by surface buoyancies that vary only in the Cartesian X direction. These flows are two-dimensional in a slab-symmetric sense. With U interpreted as the X-velocity component, and D as a lateral (in X) length scale, (2.1)–(2.3) and (2.5) still hold, but with X in place of R, while (2.4) and (2.6) apply in modified forms with $\partial U/\partial X$ replacing $1/R\,\partial/\partial R\,(RU)$. Variables are again non-dimensionalized using (2.8)–(2.10), but with the relation for r replaced by $x \equiv X/D$. The equation analogous to (2.13) is

$$\frac{\partial^6 u}{\partial z^6} + \frac{\partial^2 u}{\partial x^2} = 0. \quad (3.1)$$

We solve (3.1) using the method of Fourier transforms (e.g., DB). The Fourier sine transform $\hat{q}^s(k,z)$ and cosine transform $\hat{q}^c(k,z)$ of a function $q(x,z)$, and the corresponding inversion formulae are

$$\hat{q}^s(k,z) \equiv \sqrt{\frac{2}{\pi}}\int_0^\infty q(x,z)\sin(kx)dx, \quad q(x,z) = \sqrt{\frac{2}{\pi}}\int_0^\infty \hat{q}^s(k,z)\sin(kx)dk. \quad (3.2)$$

$$\hat{q}^c(k,z) \equiv \sqrt{\frac{2}{\pi}}\int_0^\infty q(x,z)\cos(kx)dx, \quad q(x,z) = \sqrt{\frac{2}{\pi}}\int_0^\infty \hat{q}^c(k,z)\cos(kx)dk. \quad (3.3)$$

Multiplying (3.1) by $\sin(kx)$, and integrating the resulting equation with respect to x from $x=0$ to $x=\infty$, (considering u to vanish as $x\to 0$ and as $x\to\infty$, and $\partial u/\partial x$ to vanish as $x\to\infty$) yields

$$\frac{d^6\hat{u}^s}{dz^6} - k^2\hat{u}^s = 0. \quad (3.4)$$

Since (3.4) is identical to (2.17), the general solutions for $\hat{u}^s$ and $\hat{u}^1$ are identical. Since a_i in the general solution for $\hat{u}^s$ satisfy (2.20) and (2.21), the relationship (2.24) also applies in the slab-symmetric case, and the equation analogous to (2.22) ($d^3\hat{u}^s/dz^3 + k\hat{b}^c = 0$) yields an equation analogous to (2.23) [$a_4 - a_5 - a_6 = \hat{f}^c$, where $\hat{f}^c \equiv \int_0^\infty f(x)\ \cos(kx)\,dx$], the particular solutions for $\hat{u}^1$, $\hat{b}^0$, and $\hat{w}^0$ carry over with minor notational changes as the particular solutions for $\hat{u}^s$, $\hat{b}^c$, and $\hat{w}^c$. Accordingly, the only differences between the axisymmetric and slab-symmetric solutions arise from generic differences between Hankel and Fourier transforms.

In slab-symmetric flows, isolines of the planar stream function ψ (same symbol is used for planar and Stokes stream functions) coincide with streamlines (e.g., Kundu and Cohen [47]). This stream function satisfies $u = \partial\psi/\partial z$ and $w = -\partial\psi/\partial x$. Multiplying the latter equation by $\cos(kx)$ and integrating the result with respect to x yields

$$\hat{\psi}^s = -\frac{1}{k}\hat{w}^c. \quad (3.5)$$

By taking the appropriate inverse transforms we are led to the slab-symmetric solutions:

$$u = \sqrt{\frac{2}{\pi}} \int_0^\infty \sin(kx)\hat{f}^c \left[\frac{1}{2} e^{-k^{1/3}z} - \frac{1}{\sqrt{3}} e^{-k^{1/3}z/2} \cos\left(\frac{\sqrt{3}}{2} k^{1/3} z - \frac{\pi}{6} \right) \right] dk, \quad (3.6)$$

$$b = \sqrt{\frac{2}{\pi}} \int_0^\infty \cos(kx)\hat{f}^c \left[\frac{1}{2} e^{-k^{1/3}z} + \frac{1}{\sqrt{3}} e^{-k^{1/3}z/2} \cos\left(\frac{\sqrt{3}}{2} k^{1/3} z - \frac{\pi}{6} \right) \right] dk, \quad (3.7)$$

$$w = \sqrt{\frac{2}{\pi}} \int_0^\infty k^{2/3} \cos(kx)\hat{f}^c \left[\frac{1}{2} e^{-k^{1/3}z} - \frac{1}{\sqrt{3}} e^{-k^{1/3}z/2} \cos\left(\frac{\sqrt{3}}{2} k^{1/3} z + \frac{\pi}{6} \right) \right] dk, \quad (3.8)$$

$$p = -\sqrt{\frac{2}{\pi}} \int_0^\infty k^{-1/3} \cos(kx)\hat{f}^c \left[\frac{1}{2} e^{-k^{1/3}z} + \frac{1}{\sqrt{3}} e^{-k^{1/3}z/2} \cos\left(\frac{\sqrt{3}}{2} k^{1/3} z + \frac{\pi}{6} \right) \right] dk, \quad (3.9)$$

$$\psi = -\sqrt{\frac{2}{\pi}} \int_0^\infty k^{-1/3} \sin(kx)\hat{f}^c \left[\frac{1}{2} e^{-k^{1/3}z} - \frac{1}{\sqrt{3}} e^{-k^{1/3}z/2} \cos\left(\frac{\sqrt{3}}{2} k^{1/3} z + \frac{\pi}{6} \right) \right] dk. \quad (3.10)$$

4 Examples

In this section we examine flows induced by surface buoyancies that vary as the Gaussian functions $f = \exp(-R^2/D^2) = \exp(-r^2)$ and $f = \exp(-X^2/D^2) = \exp(-x^2)$, and the parabolic arch functions $f = (1 - r^2)H(1 - r)$ and $f = (1 - x^2)H(1 - |x|)$, where $H(\chi)$ is a Heaviside unit step function of χ ($\equiv 0$ for $\chi < 0$; $\equiv 1$ for $\chi > 0$). As seen in Fig. 1, these functions are similar near the city center but diverge as the city limit is approached through increasing x (r), with the buoyancy gradient gradually decaying in the Gaussian function case but rapidly increasing in the parabolic arch function case. We also briefly discuss below the rectangle function case considered by K75 and others.

The solutions are evaluated on an analysis grid with a grid spacing of Δx (Δr) $= \Delta z = 0.02$. The analysis domain is large enough to include the primary in-up-out circulation (circulation whose inflowing branch is adjacent to the Earth's surface), but does not include any of a succession of progressively (much) weaker overlying circulations that extends to $z \to \infty$.

4.1 Gaussian function

We first examine the Gaussian function cases. The axisymmetric function has the zero order Hankel transform (Table B-5 of DB)

$$\hat{f}^0 = \int_0^\infty e^{-r^2} r J_0(kr)\, dr = \frac{1}{2} e^{-k^2/4}, \quad (4.1)$$

and the slab-symmetric function has the Fourier cosine transform (Table B-2 of DB)

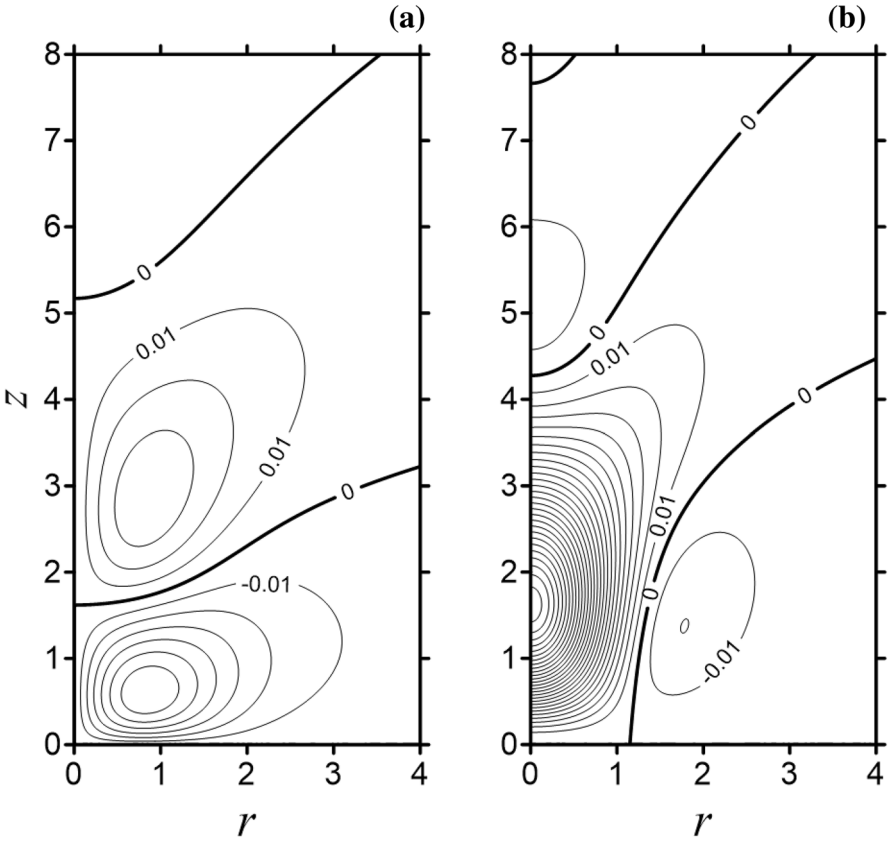

Fig. 2 Vertical $(r - z)$ plots of **a** u and **b** w for flow induced by an axisymmetric Gaussian forcing function. All quantities are non-dimensional. Contour increments for u and w are 0.01

$$\hat{f}^c = \sqrt{\frac{2}{\pi}} \int_0^\infty \mathrm{e}^{-x^2} \cos(kx)\, dx = \frac{1}{\sqrt{2}} \mathrm{e}^{-k^2/4}. \tag{4.2}$$

The integrals in (2.30)–(2.33) and (2.37) with $\hat{f}^0$ given by (4.1), and (3.6)–(3.10) with $\hat{f}^c$ given by (4.2) are evaluated numerically using the trapezoidal rule with a wavenumber increment of $\Delta k = 0.0025$ and the upper limit of integration truncated at $k = 10$. Due to the rapid decays of $\hat{f}^0$ and $\hat{f}^c$ with k in (4.1) and (4.2), the errors committed with this truncation are insignificant. The Bessel functions are evaluated with their ascending series representations [(9.1.10) of AS] for kr $(kx) \leq 8$, and their Hankel asymptotic expansions [(9.2.5) of AS] for kr $(kx) > 8$.

The u and w fields for the axisymmetric case are shown in Fig. 2, and the ψ and b fields are shown in Fig. 3. The corresponding slab-symmetric fields are shown in Figs. 4 and 5. Information about the local extrema in these cases is given in Table 1. Some structural flow features are common to both geometries. The flow is dominated by an in-up-out circulation in which the peak updraft speed w_{up} is an order of magnitude larger than the peak speed of

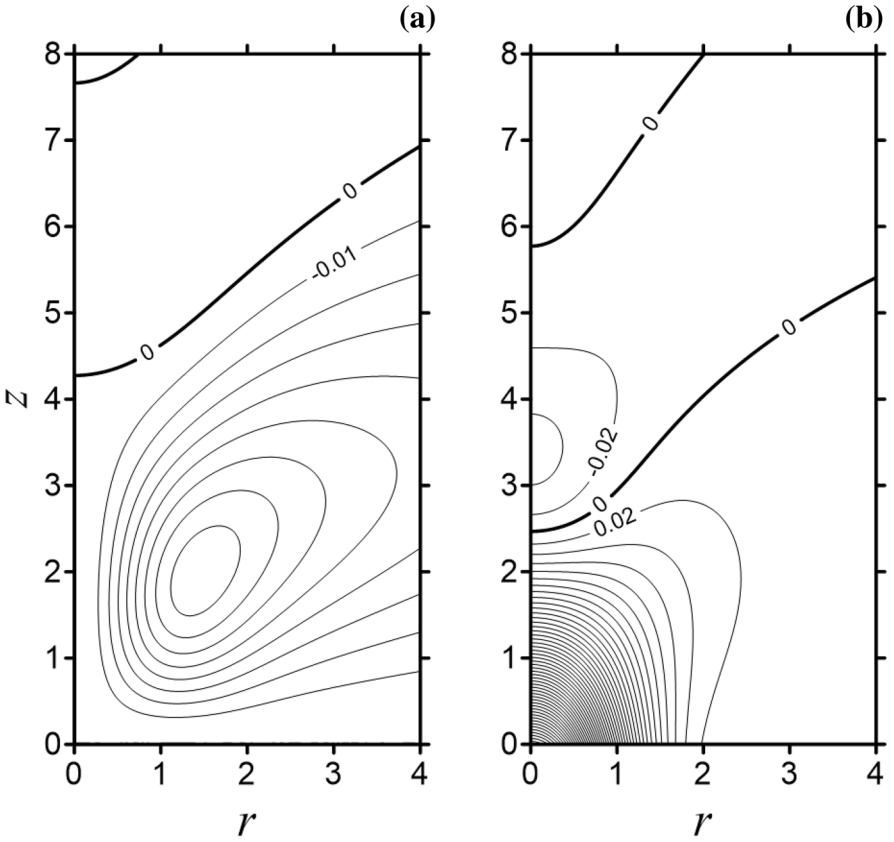

Fig. 3 Vertical $(r - z)$ plots of **a** ψ and **b** b for flow induced by an axisymmetric Gaussian forcing function. All quantities are non-dimensional. Contour increment for ψ is 0.01. Contour increment for b is 0.02

the surrounding downdraft w_{down}. The inflow branch of the circulation gradually descends as $x\,(r)$ decreases for $x\,(r) > 1$, before turning upward in the vicinity of the city limit. The downdraft is strongest in the vicinity of $x\,(r) \sim 1.75$, in a region of unremarkable buoyancy gradient. Crossover layers of negative buoyancy are found along the central axis and in the rising portion of the outflowing branch of the circulation, although the peak magnitudes of buoyancy in these layers are just a few per cent of the peak surface buoyancy. A number of differences related to geometry, however, are also evident. The central updraft is more than 40% stronger in the axisymmetric case than in the slab-symmetric case, while the surrounding downdraft (albeit rather weak), is more than 150% stronger in the slab-symmetric case than in the axisymmetric case. The peak inflow and outflow wind speeds, u_{in} and u_{out}, are both higher in the slab-symmetric case (~35% higher for u_{in} and ~28% higher for u_{out}). Within the inflow branch of the circulation, for $x\,(r) > \sim 1.8$ in the axisymmetric case and $x\,(r) > \sim 1.5$ in the slab-symmetric case, there is a slight tendency for the buoyancy to increase with height. The effect is more pronounced in the slab-symmetric case, which can be attributed to the greater subsidence warming associated with the stronger downdraft in that case. Similarly, the larger magnitudes of the negative buoyancies in the crossover layer

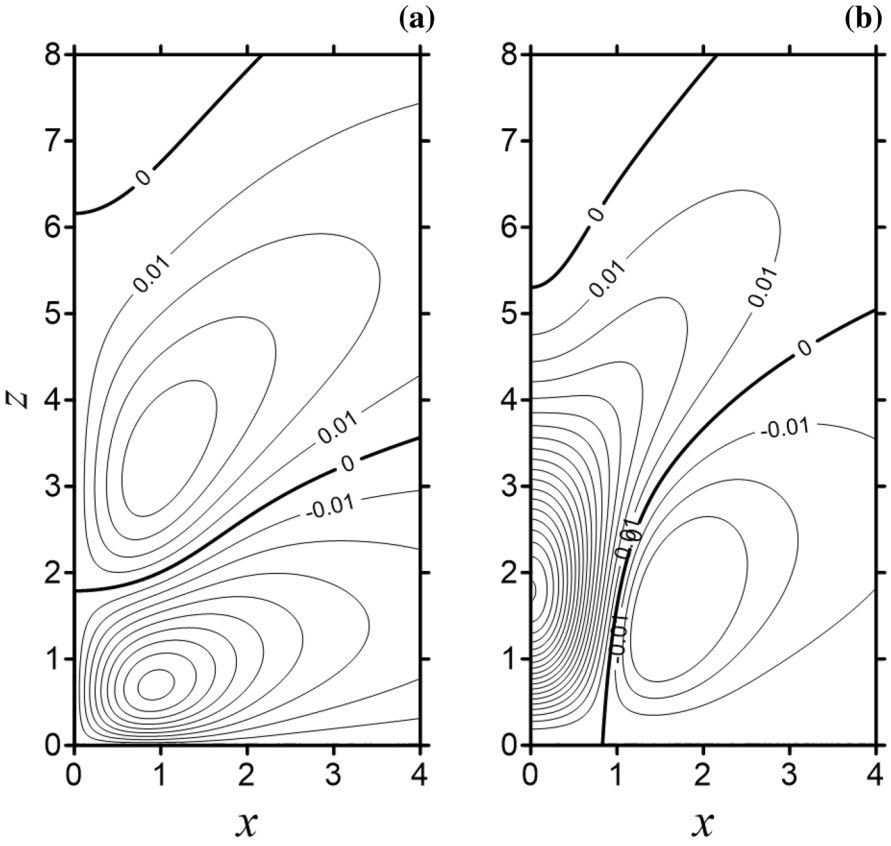

Fig. 4 Vertical $(x - z)$ plots of **a** u and **b** w for flow induced by a slab-symmetric Gaussian forcing function. All quantities are non-dimensional. Contour increments for u and w are 0.01

(particularly over the city center) in the axisymmetric case can be attributed to adiabatic cooling in the stronger updraft.

4.2 Parabolic arch function

Next, we consider the parabolic arch cases. The axisymmetric function $f = (1 - r^2)H(1 - r)$ has the zero order Hankel transform (Table B-5 of DB)

$$\hat{f}^0 = \int_0^\infty (1 - r^2)H(1 - r)\, r J_0(k r)\, dr = \frac{4}{k^3} J_1(k) - \frac{2}{k^2} J_0(k). \tag{4.3}$$

For the slab-symmetric case we use Table B-2 of DB to write the Fourier cosine transform of $f = (1 - x^2)^{\mu - 1/2} H(1 - x)$ (our particular function corresponds to $\mu = 3/2$) as

$$\hat{f}^c = \sqrt{\frac{2}{\pi}} \int_0^\infty (1 - x^2)^{\mu - 1/2} H(1 - x) \cos(k x)\, dx = 2^{\mu - 1/2}\, \Gamma(\mu + 1/2)\, k^{-\mu} J_\mu(k). \tag{4.4}$$

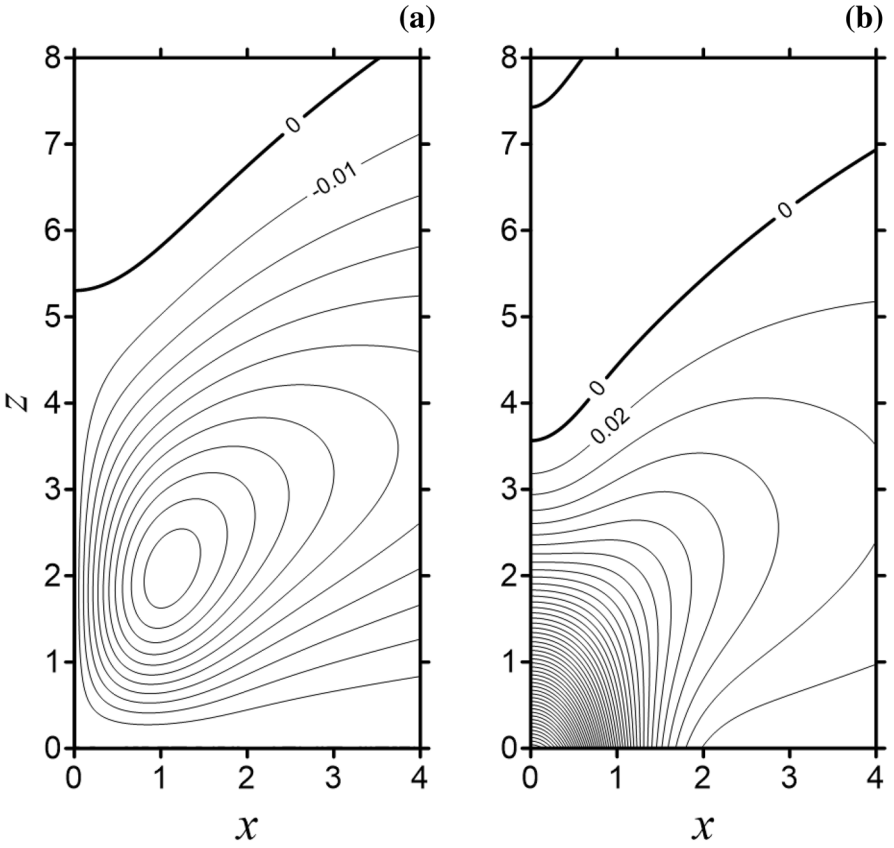

Fig. 5 Vertical $(x - z)$ plots of **a** ψ and **b** b for flow induced by a slab-symmetric Gaussian forcing function. All quantities are non-dimensional. Contour increment for ψ is 0.01. Contour increment for b is 0.02

Setting $\mu = 3/2$ in (4.4) and noting that $J_{3/2}(k) = \sqrt{2k/\pi}\,(\sin k/k^2 - \cos k/k)$ [using (10.1.1) and (10.1.11) of AS], we obtain the transform as

$$\hat{f}^c = 2\sqrt{\frac{2}{\pi}}\left(\frac{\sin k}{k^3} - \frac{\cos k}{k^2}\right). \tag{4.5}$$

We again evaluate the solution integrals using the trapezoidal rule with a wavenumber increment of $\Delta k = 0.0025$, and appropriate series and asymptotic representations for the Bessel functions. However, because of the relatively slow decays of $\hat{f}^0$ and $\hat{f}^c$ with k [compare (4.3) and (4.5) to (4.1) and (4.2)], it was necessary to truncate the integrals at a much higher value of k. A cutoff value of $k \sim 1300$ was deemed sufficiently large as further increases produced no discernable changes to the solution.

Results obtained with parabolic arch forcing in axisymmetric geometry are shown in Figs. 6 and 7, and in slab-symmetric geometry in Figs. 8 and 9. Overall, the main flow structures arising from parabolic arch forcing are similar to those arising from Gaussian forcing for both axisymmetric and slab-symmetric geometries. An important difference,

Table 1 Characteristics of UHICs in axisymmetric and slab-symmetric geometries

	Axisymmetric Gaussian	Slab-symmetric Gaussian	Axisymmetric parabolic arch	Slab-symmetric parabolic arch
w_{up}	0.276	0.191	0.316	0.219
z_{up}	1.62	1.78	1.60	1.76
w_{down}	− 0.020	− 0.051	− 0.152	− 0.187
z_{down}	1.38	1.54	0.64	0.78
x_{down} (r_{down})	1.78	1.60	1.00	1.00
u_{in}	− 0.069	− 0.094	− 0.088	− 0.116
z_{in}	0.60	0.70	0.54	0.60
x_{in} (r_{in})	0.84	0.94	0.78	0.82
u_{out}	0.038	0.049	0.048	0.057
z_{out}	2.88	3.30	2.54	2.88
x_{out} (r_{out})	0.86	0.98	0.72	0.74
z_{cross}	2.48	3.58	2.26	3.18

In all cases the updraft is strongest on the central axis, x (r) = 0. The peak values of w in the updraft and downdraft are denoted by w_{up} (> 0) and w_{down} (< 0), respectively. The peak values of u in the inflow and outflow branches of the circulation are denoted by u_{in} (< 0) and u_{out} (> 0), respectively. The height of the peak inflow is z_{in}; analogous notation is used for the locations of other extrema. The height of the crossover point (height of zero buoyancy) on the central axis is z_{cross}. All quantities are non-dimensional

however, is that in the parabolic arch forcing cases, the peak downdraft in both geometries is much more intense and its location is shifted inward (now over the city limit) and downward. This downdraft is found in association with an intense baroclinic zone. As in the Gaussian cases, the axisymmetric updraft is stronger than the slab-symmetric updraft, while the downdraft and the inflow/outflow branches of the slab-symmetric circulation are stronger than in the axisymmetric circulation.

4.3 Rectangle function

A particularly simple surface buoyancy function—the rectangle function $f = H(1 - |x|)$ or its axisymmetric equivalent—has been used in idealized numerical [15, 21, 43, 45, 57] and laboratory [43, 45, 51, 52, 56] simulations of oceanic and urban heat islands. K75 presented a linear analytical solution for the perturbation temperature and wind field for this case but did not graph the latter. We briefly comment on that wind field. The Fourier cosine transform of $f = H(1 - |x|)$ is given in Table B-2 of DB as

$$\hat{f}^c = \sqrt{\frac{2}{\pi}} \int_0^\infty H(1-x)\ \cos(kx)\, dx = \sqrt{\frac{2}{\pi}} \frac{\sin k}{k}. \tag{4.6}$$

In this case, progressively increasing the upper limit of integration in the truncated form of (3.6) decreased the height of the wind maximum to the point where it eventually reached the first grid point above the ground, just over the buoyancy discontinuity. We conjectured that the analytical solution might actually describe a wind maximum adjacent to the ground, which would be associated with infinite shear. This was confirmed by setting z=0 and x=1 in the

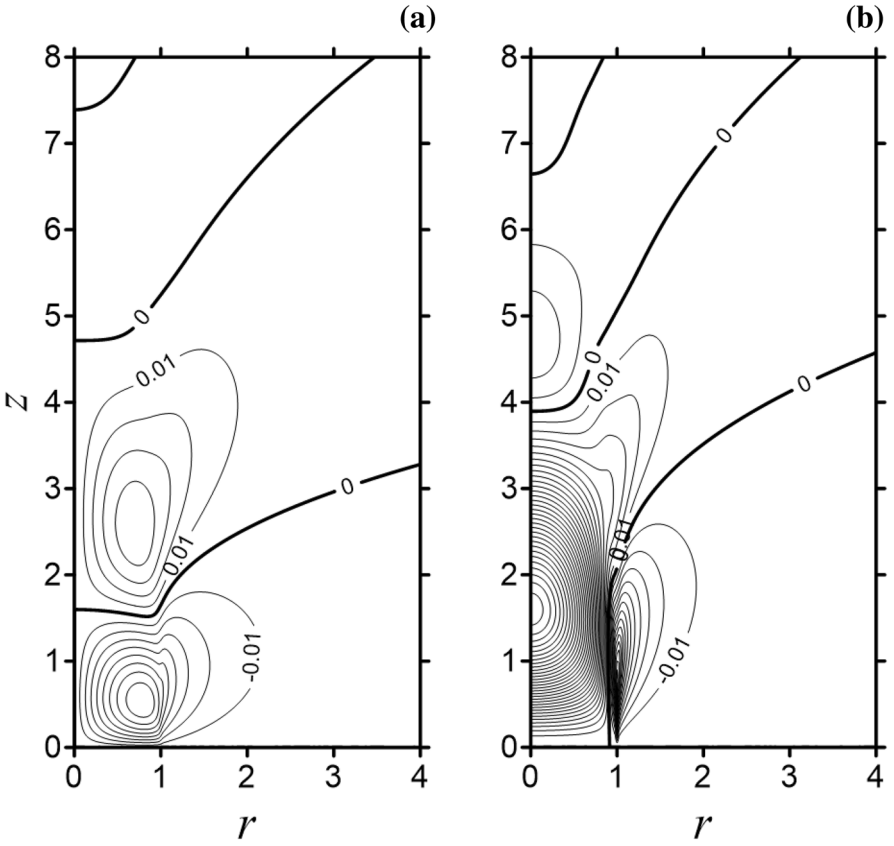

Fig. 6 As in Fig. 2, but for u and w in flow induced by an axisymmetric parabolic arch forcing function

vertical derivative of (3.6), and using the fact that $\int_0^\infty k^{-2/3}\cos(2k)dk$ is finite [(858.813) of Dwight [18]] while $\int_0^\infty k^{-2/3}dk = 3k^{1/3}\big|_0^\infty$ is infinite:

$$\left.\frac{\partial u}{\partial z}\right|_{\substack{x=1\\z=0}} = \frac{1}{\pi}\int_0^\infty \frac{\sin^2 k}{k^{2/3}}dk = \frac{1}{2\pi}\int_0^\infty \frac{1-\cos(2k)}{k^{2/3}}dk = \infty. \tag{4.7}$$

To avoid such singular behavior, we have specifically worked with continuous surface buoyancy distributions (i.e., Gaussian and parabolic arch functions). We note that prior to the K75 study, Vukovich [80] had suggested that the strong winds produced by some idealized heat island models were due to the near-infinite lateral temperature gradients in those models, but that realistic urban heat islands away from bodies of water should have smoothly varying temperature fields.

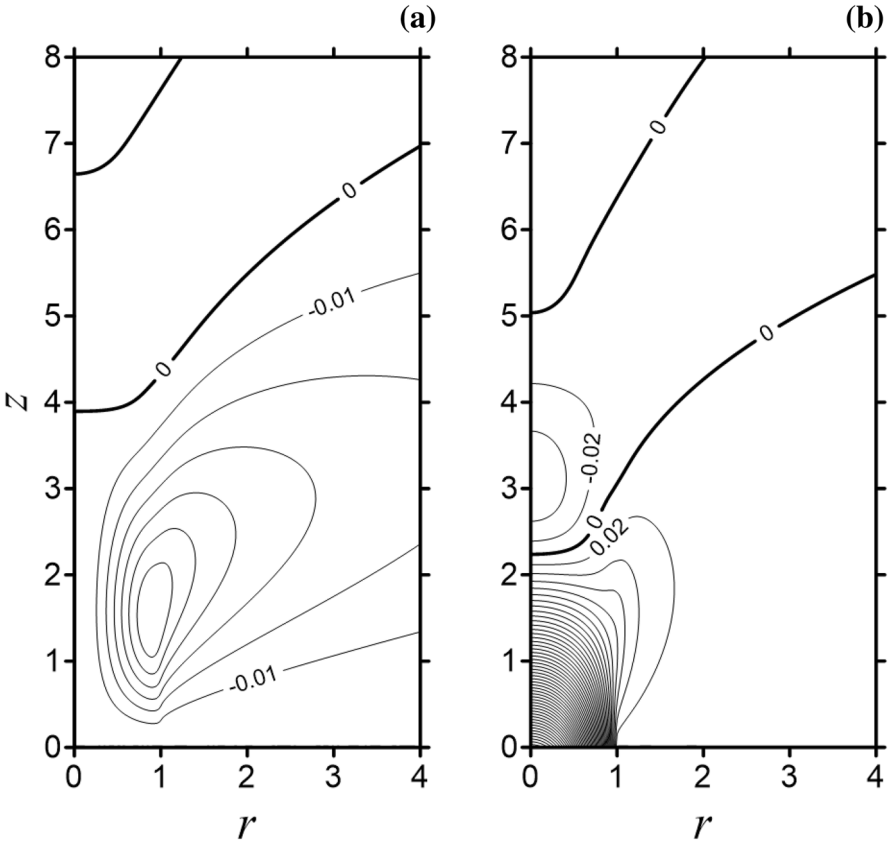

Fig. 7 As in Fig. 3, but for ψ and b in flow induced by an axisymmetric parabolic arch forcing function

5 Discussion

5.1 Impact of forcing geometry on circulation strength

Our study shows that flow geometry has different impacts on the different branches of the UHIC. For both Gaussian and parabolic arch function forcings, the updraft is stronger in the axisymmetric case, while the downdraft and horizontal branches of the circulation are stronger in the slab-symmetric case. Similar results for the vertical velocity field are obtained in a modeling study of cumulus clouds by Soong and Ogura [72]: the simulated updraft is stronger in the axisymmetric model than in the slab-symmetric model, and the ratio of the peak downdraft speed to peak updraft speed is much greater in the slab-symmetric model. In explaining these results, Soong and Ogura [72] noted that the (downward) vertical perturbation pressure gradient force (PPGF) in the core region of the simulated clouds opposed the buoyancy forcing, and that the effect was much larger in the slab-symmetric model. Similarly, in an analytical study of cumulus convection, Yau [83] found that the PPGF opposing the cloud buoyancy forcing was almost twice as large in the slab-symmetric case than in the axisymmetric case. In a study of dry thermal convection, Rambaldi and Randall [65] found that axisymmetric thermals rose faster than slab-symmetric

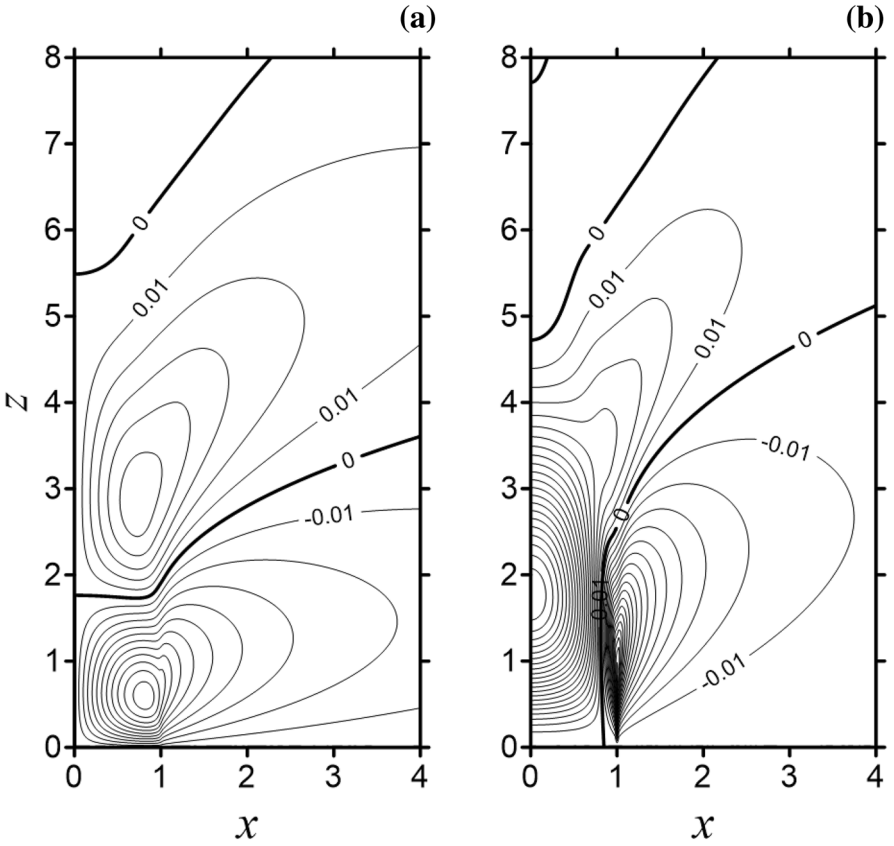

Fig. 8 As in Fig. 4, but for u and w in flow induced by a slab-symmetric parabolic arch forcing function

thermals because the former could push through its environment more easily—the environmental air could be displaced in two dimensions in the axisymmetric case but only one dimension in the slab-symmetric case. Similarly, in a study of dry ellipsoidal thermal bubbles, Shapiro and Kanak [67] found that buoyant elements with a fixed vertical length scale developed a stronger downward-directed vertical PPGF (i.e., one that opposed the buoyancy) for larger horizontal length scales. This indicated that the environment offered greater resistance to buoyant ascent for wider (more laterally extensive) bubbles.

In the present study we can infer from the spacing of isolines of the perturbation pressure field π (shown in Fig. 10 for the Gaussian functions) that there is a stronger downward-directed vertical PPGF $-\partial\pi/\partial z$ in the slab-symmetric case than in the axisymmetric case for all x (r) in a deep layer ($\sim 1 < z < \sim 2.5$) that contains the updraft and downdraft speed maxima. This downward-directed force weakens the updraft but strengthens the downdraft. Additionally, we can infer from Fig. 10 that the stronger horizontal PPGF, evident at most locations in the slab-symmetric case, strengthens the inflow at low levels and the outflow at upper levels.

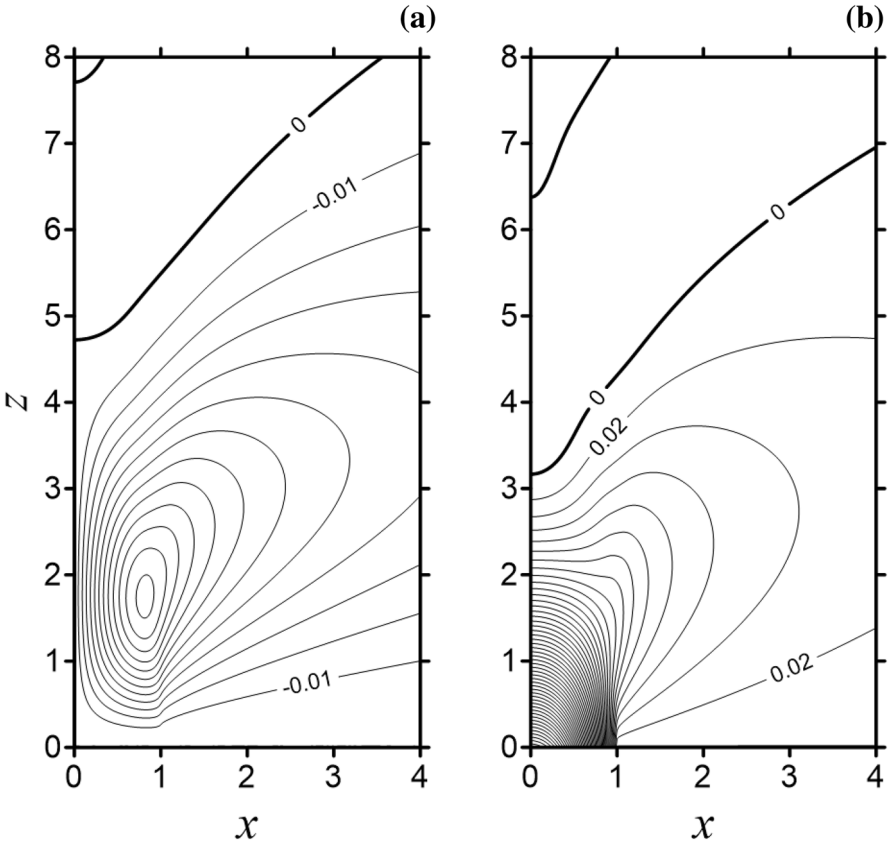

Fig. 9 As in Fig. 5, but for ψ and b in flow induced by a slab-symmetric parabolic arch forcing function

5.2 Implications of the scalings for the timing of the peak circulation strength

We now examine how the strength of the circulation is affected by the scalings (2.7)-(2.9) (and slab-symmetric equivalents). As we have seen, use of these scalings to non-dimensionalize variables has yielded a problem with no external parameters, and solutions that are universal [also noted by Niino et al. [56] for the linearized version of their problem]. In view of these scalings, the dimensional peak inflow speed U_{in}, peak updraft speed W_{up}, and height of peak updraft Z_{up} can be written as

$$U_{\mathrm{in}} = U_0\, u_{in} = \frac{B_0}{N\,\mathrm{Pr}^{1/2}} u_{in}, \tag{5.1}$$

$$Z_{\mathrm{up}} = H\, z_{\mathrm{up}} = \frac{\nu^{1/3} D^{1/3}}{N^{1/3}\,\mathrm{Pr}^{1/6}} z_{\mathrm{up}}, \tag{5.2}$$

$$W_{\mathrm{up}} = W_0\, w_{\mathrm{up}} = \frac{B_0\, \nu^{1/3}}{N^{4/3} D^{2/3}\,\mathrm{Pr}^{2/3}} w_{\mathrm{up}}, \tag{5.3}$$

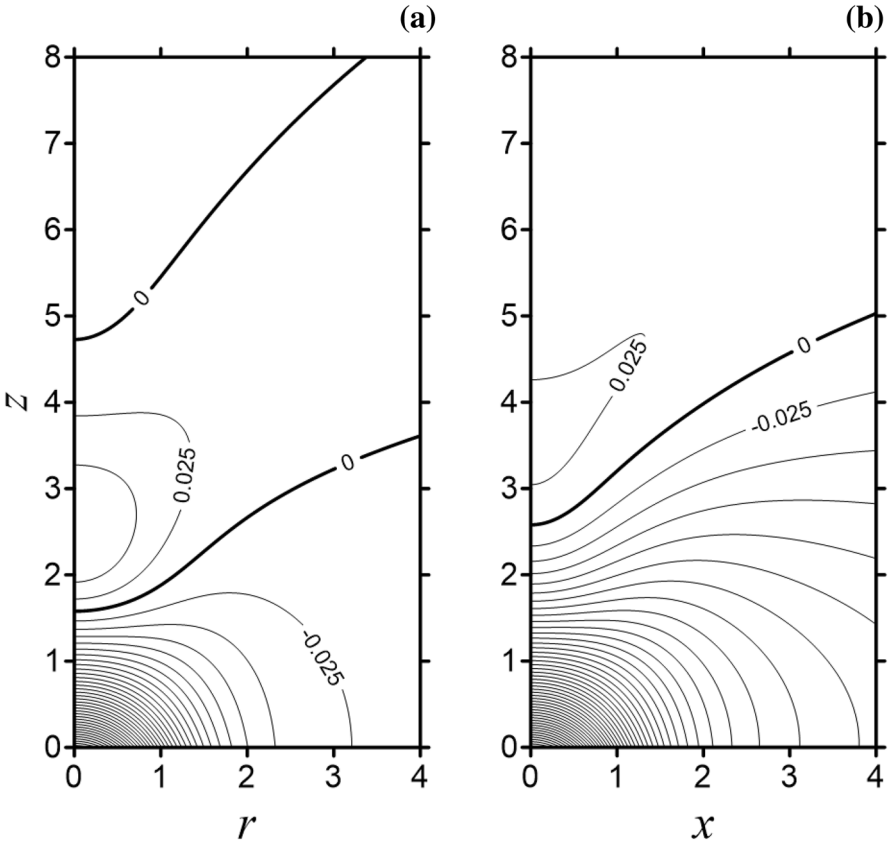

Fig. 10 Vertical plots of the kinematic perturbation pressure p for flows induced by Gaussian forcing functions in **a** axisymmetric and **b** slab-symmetric configurations. All quantities are non-dimensional. Contour increment is 0.025

with analogous equations for the peak outflow speed U_{out}, height of the peak downdraft Z_{down}, and peak downdraft speed W_{down}. Not surprisingly, an increasing stable stratification (quantified by larger N), by itself, weakens the updraft/downdraft and the inflow/outflow currents. Similarly, a decreasing urban–rural temperature contrast (quantified through smaller B_0), by itself, also weakens the overall circulation.

Typical day-to-night changes in the turbulence characteristics of the boundary layer can have a large impact on the velocity and vertical length scales in (2.8) and (2.9) [(5.1)–(5.3)], and may provide insight into the tendency, noted in Sect. 1, for some UHICs to be stronger during the day, despite the urban–rural temperature contrasts being larger at night. During the day, under conditions of vigorous dry convective mixing, ν can range from $\sim 10\ \text{m}^2\ \text{s}^{-1}$ to $\sim 100\ \text{m}^2\ \text{s}^{-1}$ [13, 76, 82], while Pr is generally less than 1 and can be as low as ~ 0.3 in a very unstable regime[3] [10, 32, 79]. In contrast, in stable conditions, ν typically ranges from

[3] Of course, for ν to be large during the day while Pr is small (less than 1), the daytime thermal diffusivity κ must be very large (i.e., exceed the value of ν).

Table 2 Sensitivity of a UHIC to surface buoyancy and mixing parameters

	B_0 (m s^{-2})	ν (m^2 s^{-1})	Pr	H (m)	U_0 (m s^{-1})	W_0 (m s^{-1})	Z_{up} (m)	U_{in} (m s^{-1})	W_{up} (m s^{-1})
Night N1	0.2	1	1	126	20.0	0.126	224	− 1.88	0.024
Night N2	0.2	1	10	86	6.3	0.027	153	− 0.59	0.005
Day D1	0.06	10	1	271	6.0	0.081	482	− 0.56	0.016
Day D2	0.06	10	0.3	332	11.0	0.181	591	− 1.03	0.035
Day D3	0.06	50	0.3	567	11.0	0.311	1009	− 1.03	0.059

The UHIC is forced by a slab-symmetric Gaussian surface buoyancy function. The peak inflow speed U_{in}, height of peak updraft Z_{up}, and peak updraft speed W_{up} are calculated from (5.1)–(5.3) with parameters: $N = 0.01$ s^{-1}, $D = 20$ km, $B_0 = 0.06$ m s^{-2} (day) and 0.2 m s^{-2} (night), corresponding to urban–rural temperature contrasts of ~1.8 K and ~6 K, respectively, $u_{in} = -0.094$, $z_{up} = 1.78$, and $w_{up} = 0.191$ (from Table 1), and ν and Pr as indicated in the Table above

~ 0.01 m^2 s^{-1} to ~ 1 m^2 s^{-1} [13, 53, 68, 82], while Pr can vary from near 1 to over 100 [37, 46, 48, 79]. From (2.8) and (2.9) we see that the smaller value of Pr (e.g., Pr = 0.3) during the day would, by itself, tend to increase U_0, H, and W_0 over their nighttime values, thus compensating for the smaller daytime B_0. This daytime Prandtl number effect is the strongest for the W_0 scale. We also see that a much larger daytime value of ν, by itself, results in larger daytime values of H and W_0. However, this daytime eddy viscosity effect does not extend to U_0. The reason W_0 receives the overall largest increases can be understood from the relation $W_0 = U_0 H / D$ (consistent with the scaled incompressibility condition), which indicates that W_0 accrues the gains obtained by H and U_0. However, since there is no daytime eddy viscosity effect on U_0, only Prandtl number effects can explain a daytime maximum in U_0, at least within the framework of our theory. Examples of UHICs forced by a slab-symmetric Gaussian surface buoyancy function are shown in Table 2. There we see cases where the updraft and inflow current are strongest at night (D1 vs. N1) or strongest during the day (D2 and D3 vs. N2). We also see cases where the updraft is strongest during the day but the inflow is strongest at night (D1 vs. N2, D2 and D3 vs. N1).

6 Summary and conclusion

We have revisited a linearized model of steady shallow convective flow of a viscous stably stratified fluid over a differentially heated lower boundary without Coriolis force or background wind, a problem of relevance to heat island circulations (urban or oceanic) considered by K75 and others. Solutions of the linearized coupled equations of motion and thermal energy were obtained for surface buoyancy functions that varied as Gaussian and parabolic arch functions. The flows were modeled in axisymmetric and slab-symmetric frameworks.

In all cases the dominant flow is an in-up-out circulation. The updraft is strongest along the axis of symmetry. The surrounding downdraft is much weaker than the updraft in the Gaussian function forced cases, but becomes almost as strong as the updraft in the parabolic arch function forcing cases. In all cases a crossover layer of weak negative buoyancies is present at upper levels along the central axis and in the rising outflow branch of the circulation.

For both Gaussian and parabolic arch function forcings, the central updraft is stronger in the axisymmetric case, while the surrounding downdraft and horizontal branches of the circulation are stronger in the slab-symmetric case. These features arise from the increased magnitude of the PPGF that develops in the slab-symmetric geometry: the downward-directed vertical component of the PPGF in a layer with the peak updraft and downdraft intensities, the inward-directed lateral component of the horizontal PPGF in the inflow layer, and the outward-directed lateral component of the horizontal PPGF in the outflow layer are all stronger in the slab-symmetric geometry.

The power-law scalings deduced in our analysis may explain why the daytime UHIC can be stronger than the nighttime UHIC despite the relative weakness of urban–rural temperature contrasts during the daytime. A smaller daytime turbulent Prandtl number (consistent with smaller Pr observed in very unstable regimes, e.g., $\mathrm{Pr}=0.3$) would, by itself, force a more vigorous updraft and inflow current than would occur at night with a larger Prandtl number more representative of a neutral or stable regime. Additionally, a larger value of eddy viscosity during the day would, by itself, force a more intense updraft during the day. The intensities of UHICs were evaluated for surface buoyancy and turbulent mixing parameters characteristic of daytime and nighttime conditions. Examples were given of circulations that were strongest during the day and strongest during the night. Additionally, circulation cases were found in which the updraft was strongest during the day but the inflow was strongest at night. The sensitivity of our simple model solutions seen in these results suggests that the detailed turbulence characteristics of flows in the urban setting may play an important and potentially complex role in determining the overall strength of UHICs and the relative strengths of the horizontal and vertical velocities within those circulations.

Acknowledgements The authors thank the anonymous reviewers for their helpful comments.

References

1. Abramowitz M, Stegun IA (eds) (1972) Handbook of mathematical functions. US Department of Commerce, Washington
2. Arnfield AJ (2003) Two decades of urban climate research: a review of turbulence, exchanges of energy and water, and the urban heat island. Int J Climatol 23:1–26
3. Baik J-J (1992) Response of a stably stratified atmosphere to low-level heating: an application to the heat island problem. J Appl Meteorol 31:291–303
4. Baik J-J, Chun H-Y (1997) A dynamical model for urban heat islands. Bound-Layer Meteorol 83:463–477
5. Barlag A-B, Kuttler W (1990/1991) The significance of country breezes for urban planning. Energy Build 15–16: 291–297
6. Bornstein RD (1968) Observations of the urban heat island effect in New York City. J Appl Meteorol 7:575–582
7. Bornstein RD, Johnson DS (1977) Urban-rural wind velocity differences. Atmos Environ 11:597–604
8. Bornstein RD (1987) Mean diurnal circulation and thermodynamic evolution of urban boundary layers. In: Kramer ML (ed) Modeling the urban boundary layer. American Meteorological Society, Boston, pp 53–93
9. Bornstein R, Lin Q (2000) Urban heat islands and summertime convective thunderstorms in Atlanta: three case studies. Atmos Environ 34:507–516
10. Businger JA, Wyngaard JC, Izumi Y, Bradley EF (1971) Flux-profile relationships in the atmospheric surface layer. J Atmos Sci 28:181–189
11. Cenedese A, Monti P (2003) Interaction between an inland urban heat island and a sea- breeze flow: a laboratory study. J Appl Meteorol 42:1569–1583

12. Cui YY, de Foy B (2012) Seasonal variations of the urban heat island at the surface and the near-surface and reductions due to urban vegetation in Mexico City. J Appl Meteorol Climatol 51:855–868
13. Dandou A, Tombrou M, Schäfer K, Emeis S, Protonotariou AP, Bossioli E, Soulakellis N, Suppan P (2009) A comparison between modelled and measured mixing-layer height over Munich. Bound-Layer Meteorol 131:425–440
14. Debnath L, Bhatta D (2015) Integral transforms and their applications, 3rd edn. CRC Press, Boca Raton
15. Delage Y, Taylor PA (1970) Numerical studies of heat island circulations. Bound-Layer Meteorol 1:201–226
16. Dirks RA (1974) Urban atmosphere: warm dry envelope over St. Louis. J Geophys Res 79:3473–3475
17. Duckworth FA, Sandberg JS (1954) The effect on cities upon horizontal and vertical temperature gradients. Bull Am Meteorol Soc 35:198–207
18. Dwight HB (1961) Tables of integrals and other mathematical data. Macmillan, New York
19. Eliasson I, Holmer B (1990) Urban heat island circulation in Göteborg, Sweden. Theor Appl Climatol 42:187–196
20. Eliasson I, Upmanis H (2000) Nocturnal airflow from urban parks—implications for city ventilation. Theor Appl Climatol 66:95–107
21. Estoque MA, Bhumralkar CM (1969) Flow over a localized heat source. Mon Weather Rev 97:850–859
22. Falasca S, Moroni M, Cenedese A (2013) Laboratory simulations of an urban heat island in a stratified atmospheric boundary layer. J Vis 16:39–45
23. Fan Y, Li Y, Wang X, Catalano F (2016) A new convective velocity scale for studying diurnal urban heat island circulation. J Appl Meteorol Climatol 55:2151–2164
24. Fan Y, Hunt JCR, Li Y (2017) Buoyancy and turbulence-driven atmospheric circulation over urban areas. J Environ Sci 59:63–71
25. Fan Y, Li Y, Bejan A, Wang Y, Yang X (2017) Horizontal extent of the urban heat dome flow. Sci Rep 7:11681
26. Fernando HJS, Lee SM, Anderson J, Princevac M, Pardyjak E, Grossman-Clarke S (2001) Urban fluid mechanics: air circulation and contaminant dispersion in cities. Environ Fluid Mech 1:107–164
27. Findlay BF, Hirt MS (1969) An urban-induced meso-circulation. Atmos Environ 3:537–542
28. Freitas ED, Rozoff CM, Cotton WR, Silva Dias PL (2007) Interactions of an urban heat island and sea-breeze circulations during winter over the metropolitan area of São Paulo, Brazil. Bound-Layer Meteorol 122:43–65
29. Fujibe F, Asai T (1980) Some features of a surface wind system associated with the Tokyo heat island. J Meteorol Soc Japan 58:149–152
30. Garstang M, Tyson PD, Emmitt GD (1975) The structure of heat islands. Rev Geophys Space Phys 13:139–165
31. Gedzelman SD, Austin S, Cermak R, Stefano N, Partridge S, Quesenberry S, Robinson DA (2003) Mesoscale aspects of the Urban Heat Island around New York City. Theor Appl Climatol 75:29–42
32. Gibson MM, Launder BE (1978) Ground effects on pressure fluctuations in the atmospheric boundary layer. J Fluid Mech 86:491–511
33. Han J-Y, Baik J-J (2008) A theoretical and numerical study of urban heat island-induced circulation and convection. J Atmos Sci 65:1859–1877
34. Hidalgo J, Pigeon G, Masson V (2008) Urban-breeze circulation during the CAPITOUL experiment: observational data analysis approach. Meteorol Atmos Phys 102:223–241
35. Hidalgo J, Masson V, Pigeon G (2008) Urban-breeze circulation during the CAPITOUL experiment: numerical simulations. Meteorol Atmos Phys 102:243–262
36. Hidalgo J, Masson V, Gimeno L (2010) Scaling the daytime urban heat island and urban-breeze circulation. J Appl Meteorol Climatol 49:889–901
37. Howell JF, Sun J (1999) Surface-layer fluxes in stable conditions. Bound-Layer Meteorol 90:495–520
38. Hung T, Uchihama D, Ochi S, Yasuoka Y (2006) Assessment with satellite data of the urban heat island effects in Asian mega cities. Int J Appl Earth Obs Geoinf 8:34–48
39. Jauregui E (1988) Local wind and air pollution interaction in the Mexico basin. Atmósfera 1:131–140
40. Jeffreys H (1922) On the dynamics of wind. Q J R Meteorol Soc 48:29–47
41. Kanda M (2007) Progress in urban meteorology: a review. J Meteorol Soc Japan 85:363–383
42. Kim Y-H, Baik J-J (2002) Maximum urban heat island intensity in Seoul. J Appl Meteorol 41:651–659
43. Kimura R (1975) Dynamics of steady convections over heat and cool islands. J Meteorol Soc Japan 53:440–457
44. Kimura R (1976) Effects of general flows on a heat island convection. Part 1: linear theory for the uniform flow. J Meteorol Soc Japan 54:308–320

45. Kimura R, Misawa N, Sakagami J, Kunii TL (1977) Effects of general flows on a heat island convection. Part 2: numerical and laboratory experiments for shear flow. J Meteorol Soc Japan 55:32–51
46. Kitamura Y, Hori A, Yagi T (2013) Flux Richardson number and turbulent Prandtl number in a developing stable boundary layer. J Meteorol Soc Japan 91:655–666
47. Kundu PK, Cohen IM (2002) Fluid mechanics, 2nd edn. Academic Press, San Diego
48. Kurbatskiy AF, Kurbatskaya LI (2011) Efficiency of eddy mixing in a stable stratified atmospheric boundary layer. J Appl Mech Tech Phys 52:883–888
49. Lemonsu A, Masson V (2002) Simulation of a summer urban breeze over Paris. Bound- Layer Meteorol 104:463–490
50. Lindén J, Holmer B (2011) Thermally induced wind patterns in the Sahelian city of Ougadougou, Burkina Faso. Theor Appl Climatol 105:229–241
51. Lu J, Arya SP, Snyder WH, Lawson RE (1997) A laboratory study of the urban heat island in a calm and stably stratified environment. Part I: temperature field. J Appl Meteorol 36:1377–1391
52. Lu J, Arya SP, Snyder WH, Lawson RE (1997) A laboratory study of the urban heat island in a calm and stably stratified environment. Part II: velocity field. J Appl Meteorol 36:1392–1402
53. Mahrt L, Vickers D (2005) Extremely weak mixing in stable conditions. Bound-Layer Meteorol 119:19–39
54. Malkus JS, Stern ME (1953) The flow of a stable atmosphere over a heated island. Part 1. J Meteorol 10:30–41
55. Marques Filho EP, Cassol M, Karam HA, Rizza U (2013) The vertical structure of tropical urban heat island with LES. Am J Environ Eng 3:24–31
56. Niino H, Mori A, Satomura T, Akiba S (2006) Flow regimes of nonlinear heat island circulation. J Atmos Sci 63:1538–1547
57. Noto K (1996) Dependence of heat-island phenomena on stable stratification and heat quantity in a calm environment. Atmos Environ 30:475–485
58. Oke TR (1981) Canyon geometry and the nocturnal urban heat island: comparison of scale model and field observations. J Climatol 1:237–254
59. Oke TR (1982) The energetic basis of the urban heat island. Q J R Meteorol Soc 108:1–24
60. Oke TR (1995) The heat island of the urban boundary layer: characteristics, causes and effects. In: Cermak JE, Davenport AG, Plate EJ, Viegas DX (eds) Wind climate in cities. Kluwer, Dordrecht, pp 81–107
61. Olfe DB, Lee RL (1971) Linearized calculations of urban heat island convection effects. J Atmos Sci 28:1374–1388
62. Phelan PE, Kaloush K, Miner M, Golden J, Phelan B, Silva H, Taylor RA (2015) Urban heat island: mechanisms, implications, and possible remedies. Annu Rev Environ Resour 40:285–307
63. Pooler F (1963) Airflow over a city in terrain of moderate relief. J Appl Meteor 2:446–456
64. Poreh M (1996) Investigation of heat islands using small scale models. Atmos Environ 30:467–474
65. Rambaldi S, Randall DA (1981) Quasi-Lagrangian models of nascent thermals. Mon Weather Rev 109:1939–1951
66. Ryu Y-H, Baik J-J, Han J-Y (2013) Daytime urban breeze circulation and its interaction with convective cells. Q J R Meteorol Soc 139:401–413
67. Shapiro A, Kanak KM (2002) Vortex formation in ellipsoidal thermal bubbles. J Atmos Sci 59:2253–2269
68. Sharan M, Gopalakrishnan SG (1997) Comparative evaluation of eddy exchange coefficients for strong and weak wind stable boundary layer modeling. J Appl Meteorol 36:545–559
69. Shreffler JH (1978) Detection of centripetal heat island circulations from tower data in St. Louis. Bound-Layer Meteorol 15:229–242
70. Shreffler JH (1979) Heat island convergence in St. Louis during calm periods. J Appl Meteorol 18:1512–1520
71. Smith RC (1955) Theory of air flow over a heated land mass. Q J R Meteorol Soc 81:382–395
72. Soong S-T, Ogura Y (1973) A comparison between axisymmetric and slab-symmetric cumulus cloud models. J Atmos Sci 30:879–893
73. Stommel H, Veronis G (1957) Steady convective motion in a horizontal layer of fluid heated uniformly from above and cooled non-uniformly from below. Tellus 9:401–407
74. Tapper NJ (1990) Urban influences on boundary layer temperature and humidity: results from Christchurch, New Zealand. Atmos Environ 24B:19–27
75. Thorsson S, Eliasson I (2003) An intra-urban thermal breeze in Göteborg, Sweden. Theor Appl Climatol 75:93–104

76. Tombrou M, Dandou A, Helmis C, Akylas E, Angelopoulos G, Flocas H, Assimakopoulos V, Soulakellis N (2007) Model evaluation of the atmospheric boundary layer and mixed layer evolution. Bound-Layer Meteorol 124:61–79
77. Tyson PD, du Toit WJF, Fuggle RF (1972) Temperature structure above cities: review and preliminary findings from the Johannesburg Urban Heat Island Project. Atmos Environ 6:533–542
78. Tzavali A, Paravantis JP, Mihalakakou G, Fotiadi A, Stigka E (2015) Urban heat island intensity: a literature review. Fresenius Environ Bull 24:4537–4554
79. Ueda H, Mitsumoto S, Komori S (1981) Buoyancy effects on the turbulent transport processes in the lower atmosphere. Q J R Meteorol Soc 107:561–578
80. Vukovich FM (1971) Theoretical analysis of the effect of mean wind and stability on a heat island circulation characteristic of an urban complex. Mon Weather Rev 99:919–926
81. Vukovich FM, King WJ, Dunn JW, Worth JJB (1979) Observations and simulations of the diurnal variation of the urban heat island circulation and associated variations of the ozone distribution: a case study. J Appl Meteorol 18:836–854
82. Yamada T, Mellor G (1975) A simulation of the Wangara atmospheric boundary layer data. J Atmos Sci 32:2309–2329
83. Yau MK (1979) Perturbation pressure and cumulus convection. J Atmos Sci 36:690–694
84. Yoshikado H, Kondo H (1989) Inland penetration of the sea breeze over the suburban area of Tokyo. Bound-Layer Meteorol 48:389–407
85. Zhou B, Rybski D, Kropp JP (2013) On the statistics of urban heat island intensity. Geophys Res Lett 40:5486–5491